



1

2

3

High Resolution Simulations of Tropical Island Thunderstorms: Does an Increase in Resolution Improve the Representation of Extreme Rainfall?

4

5

6

Martin Bergemann^{*1}, Todd P. Lane^{2a}, Scott Wales^{2a}, Sugata Narsey³ and Valentin Louf^{43a}

7

¹ German Climate Computing Centre (DKRZ)

8

² School of Geography, Earth and Atmospheric Sciences, The University of Melbourne

9

³ Australian Bureau of Meteorology

10

⁴ School of Earth Atmosphere and Environment, Monash University

11

^a ARC Centre of Excellence for Climate Extremes (CLEX)

12

*Correspondence to: bergemann@dkrz.de; Deutsches Klimarechenzentrum, Bundesstraße 45a, 20146 Hamburg, Germany

13

Recent increases in computational resources have lead to the application of km and sub-km scale simulations in research, numerical weather prediction and climate modelling alike. Despite anticipated improvements with resolution, there is still considerable work needed to evaluate how well such models improve the representation of intense convection. In this study we conduct ensemble simulations with km- and sub-km scale horizontal grids to investigate intense convective events in the tropical island thunderstorm system *Hector*, which frequently occurs over the *Tiwi Islands* in North Australia. To avoid losing information through spatio-temporal averaging we apply a tracking algorithm to simulated and observed storms. When compared to observations the model storms exhibit a lack of propagation across the study domain. In general simulated storms are too intense but too small and too short lived. This is especially true for the sub-km simulations where storms are more intense, smaller and numerous than in its km-scale counterparts. We argue that size and duration errors compensate for storm number and intensity errors which could lead to wrong interpretations when only comparing time and space averages of rainfall fields. Investigating some properties of the simulated storms suggests that storms with high rainfall intensities have stronger updrafts in the sub-km model, and are accompanied by an increase in cold pool intensity. The results and their resolution sensitivities highlight that the remaining parametrizations and their many tuning parameters in high resolution setups influences the representation of convective storms in such models.

Key Words: Extreme Rainfall; High Resolution Simulation; Deep Convection

Received ...

1. Introduction

Convective storm systems in coastal areas of the tropics, such as the Maritime Continent, are of extraordinary importance for the earth climate system by distributing heat and momentum in the tropical atmosphere (Matsuno 1966; Ramage 1968; Gill 1980; Trenberth et al. 2009, and others). The geography of the Maritime Continent, with thousands of islands, plays a pivotal role in driving the tropical circulations. Yamanaka et al. (2018) showed that convective systems over the Maritime Continent contribute to roughly 20% of the global latent heat budget. Many of these convective systems are island thunderstorms which are strongly influenced by meso-scale land-sea interactions (Mori et al. 2004; Qian 2008; Bergemann et al. 2015) and can become considerably intense (Simpson et al. 1980, 1993), even if large-scale atmospheric conditions are suppressed (Bergemann and Jakob 2016).

A well known example of a tropical island thunderstorm is *Hector*. *Hector* is a single or multi cell storm system occurring frequently in the late afternoon to early evening over the Tiwi Islands, located in the south of the Timor Sea roughly 100 km north of Darwin, Australia ($11.6^{\circ}\text{S}/130.9^{\circ}\text{E}$). Its frequent occurrence over the Tiwi-Islands' rather flat terrain during the Monsoon transition season (Oct - Dec, Mar - Apr) has made *Hector* a focus of various field campaigns (Keenan et al. 1989, 2000; Vaughan et al. 2008; May et al. 2008; Leroy et al. 2016). Most notable are the Maritime Continent Thunderstorm Experiment (MCTEX, Keenan et al. 2000), the Island

29 Thunderstorm Experiment (ITEX, Keenan et al. 1989) and the Tropical Warm Pool International Cloud Experiment (TWP-ICE, May
30 et al. 2008).

31 Beringer et al. (2001) used observations from the MCTEX experiment to determine various atmospheric variables like convective
32 available potential energy or wind shear to identify four different types of Hector: 1) *Hector*, 2) *suppressed Hector*, 3) *no Hector*, and 4)
33 *late developing Hector*. They suggested that the absence of Hector (*suppressed Hector* and *no Hector*) could be either due to previously
34 traversing squall lines consuming the convective available potential energy (*suppressed Hector*) or due to an increased wind-shear (*no*
35 *Hector*). Schafer et al. (2001) took advantage of a comparatively dense network of sensors over the Tiwi Islands during MCTEX. These
36 observations were used to determine horizontal winds, mean virtual potential temperature, boundary layer depth, air temperature, and
37 convergence. Horizontal and vertical variations of these descriptors were used to characterize the development of the boundary layer.
38 These observations combined with numerical simulations showed that Hector is strongly influenced by the sea-breeze convergence
39 zones propagating the islands.

40 Crook (2001) combined observations from MCTEX with model simulations to show that low-level moisture, ambient wind speed
41 and direction play an important role in modulating the intensities of the storms. Hector events tend to increase as ambient lower level
42 wind flow decreases and the wind direction points towards the major axis of the main island. Interactions of the sea-breeze with storm
43 associated cold-pools can further modulate the occurrence, position and intensity of the Hector events.

44 High resolution convection permitting model simulations have gained an increasing popularity for investigating Hector and other
45 island thunderstorm events during the past years. Using large-eddy simulations with a resolution of 100m Dauhut et al. (2016, 2017)
46 showed that the tallest updrafts within *Hector* storm systems are able to penetrate the stratosphere. The studies suggest that reduced
47 mixing in the troposphere as well as intensification of low-level convergence lines from cold pools are crucial for the occurrence of
48 such very deep convective systems. Zhu et al. (2012) used the WRF model at 1 km horizontal resolution to simulate four Hector events
49 and described a tendency of the model to underestimate the occurrence and intensity of such events. Focusing on convective storms
50 over coastal South Africa Love et al. (2011), investigated the simulated diurnal cycle of deep island convection using the Unified Model
51 at various horizontal resolutions of up to 4.5km. They found that, compared to observations, convection over coastal land is triggered
52 early in the model, leading to a too-early peak of rainfall. This is agreement with other high resolution model simulations using the
53 WRF model (Gianotti et al. 2011; Hassim et al. 2016; Vincent and Lane 2017).

54 With the rise of convection permitting models more and more attention has been drawn to understanding convective extreme
55 events (e.g Gevorgyan 2018; Chan et al. 2014, 2013). Despite the recent efforts in model development, there is no clear consensus
56 to which degree an increase in model resolution leads to an improvement of the representation of convective extreme events in realistic
57 scenarios. For example, Jucker et al. (2020) showed with help of the UM and WRF models at both km and sub-km scale configuration,
58 that important characteristics of simulated convective systems across tropical Northern Australia do not change significantly with an
59 increase in resolution. Other rather longer-term studies using high resolution models apply some kind of spatial or temporal averaging
60 (Birch et al. 2016; Vincent and Lane 2017; Keat et al. 2019) which has also disadvantages when investigating extreme conditions.

61 The frequent occurrence of the thunderstorm system *Hector* together with its proximity to a long-running ground based dual
62 polarized research radar makes the Tiwi Islands a perfect study area to investigate intense tropical convective events. The present
63 study therefore aims at investigating intense convective over the Tiwi Islands going beyond single events while applying as little as
64 possible averaging. This is realized by investigating consecutive *Hector* events using individual thunderstorm tracks from an ensemble
65 of model simulations at different resolutions (kilometer and sub-kilometer scale). The results are then compared to ground radar based
66 observations.

67 The paper is organized as follows, sections 2-2.1 gives a short introduction to the study area while section 2-2.2 and 2-2.3 will
68 describe the ground based radar dataset and the model setup. Section 2-2.4 explains the algorithm that is applied to observational and

69 model data to track thunderstorm events in space and time. Section 3 examines the modelling results and compares them with the
 70 observations, which is followed by a discussion and conclusion in section 4.

71 **2. Model, Observations and Methods**

72 *2.1. Study Area*

73 A rigorous investigation of intense convective events simulated in cloud resolving models is a challenging task in various aspects.
 74 All statistics considering extreme events should be based on data with a sufficient sample size, because the appearance of extremes,
 75 depending its definition, is infrequent. This makes it necessary to run model simulations for longer time periods, which can become
 76 difficult given the computational complexity and large data output of cloud resolving simulations. To identify a sufficiently large sample
 77 of intense convective events that can be potentially captured by a cloud resolving model we scan radar derived rainfall observations
 78 from a 17 years record for consecutive occurrences of strong tropical coastal thunderstorm events over the Tiwi Islands in Northern
 79 Australia. This location was chosen because of the frequent occurrence of island thunderstorm systems and the availability of high
 80 quality ground radar based observations in this area. Located roughly 100 km north of Darwin, Australia the Tiwi Islands build a
 81 group of 11 mostly small islands. Their terrain is rather flat with an average height of 35 m, hills do not extent beyond 150 m (see
 82 Figure 1-a for details on location and terrain). Previous studies have hypothesized that the sizes of the two main islands - Barthurst
 83 and Meleville Island - favor the collision of two sea-breeze fronts which supports the development of deep convective storms (Crook
 84 2001; Saito et al. 2001). Hence the Tiwi Islands are subject to regular occurring island thunderstorm events. We are specifically looking
 85 for events occurring during the Monsoon build up period as defined in Narsey et al. (2017). These periods only are considered here
 86 because convection is most distinct and strongly influenced by local forcing and less by the synoptic scale forcing, which allows for
 87 a better comparison between different events. For our investigation we choose a sequence of *eight* consecutive Hector events during
 88 the Monsoon build up period from 2006-11-11 - 2006-11-19. This period is the longest sequence of successive Hector events in the
 89 entire 17 year radar archive, during Monsoon build-up and break periods defined by Narsey et al. (2017). To identify the mentioned
 90 time period we scanned the CPOL radar based precipitation estimates for consecutive, distinguishable rainfall events occurring over
 91 the Tiwi-Islands.

92 *2.2. Radar Based Observations*

93 For comparing simulated rainfall to observational data we use ground radar precipitation estimates. These estimates are based on
 94 measurements from the C-band Dual-Polarization radar (CPOL) located at Gunn Point (12.249°S; 131.044°E), roughly 65 km south
 95 of the Tiwi Islands (Keenan et al. 1998). CPOL operated at a frequency of 5.6 GHz, has an update interval of 10 minutes and a maximum
 96 range of ≈ 150 km. The dataset recently underwent a series of calibrations, quality controls and processing, which are described in
 97 detail in Louf et al. (2018). The rain-rate retrieval algorithm (Thompson et al. 2017) is applied to the data before interpolating from
 98 polar to Cartesian Coordinates with a resolution of 2.5 km in space and 10 minutes in time. The full CPOL archive runs from 1998 to
 99 2017 - with two years without operation - which is the period that was scanned to identify the November 2006 sequence of cases that
 100 are the focus of this study.

101 *2.3. Model Setup*

102 The above mentioned convective storms are being reproduced using the limited area version of the UK Met-Office's Unified Model
 103 (UM) with the *Regional Atmosphere* configuration for the *Tropics* (RA1-T; Bush et al. 2019). In a recent study Dipankar et al. (2020)
 104 observed forecasting improvements when utilizing ECMWF Analysis rather than UM Global Atmosphere (GA) data to drive a UM

105 based limited area model setup. Following this approach we force our model setup with the reanalysis ERA-Interim dataset (Berrisford
106 et al. 2011) which is made available at four daily times (0000 UTC, 0600 UTC, 1200 UTC, 1800 UTC) with a resolution of 0.75° . We
107 apply three one way nested domains at horizontal grid spacing of 4 km (UM 4km), 1.33 km (UM 1.33km) and 444 m (UM 0.44km)
108 in the smallest domain (see also Figure 1-b). The RA1-T science configuration was specifically developed for application in tropical
109 areas, with 80 vertical levels and a model top of 38.5 km. Convection parameterization is switched off in all simulations. RA1-T uses
110 a prognostic large-scale cloud scheme (Wilson et al. 2008). Sub-grid mixing is parametrized using a blend of 3D-Smagorinsky mixing
111 scheme and the more traditional Eddy-Covariance parametrization (Boutle et al. 2014). Microphysical processes are represented by the
112 Wilson and Ballard (1999) bulk microphysics scheme with prognostic liquid and ice cloud, as well as prognostic graupel and rain. The
113 4 km setup is not included in this study as it is mostly influenced by the global driving model and we wish to compare the model output
114 at the resolution of the observational dataset. Therefore we regrid the 1.33 km and 0.44 km model datasets to the 2.5 km resolution of
115 the CPOL observations using first-order conservative regridding to complete our analysis.

116 **Ensemble Simulations** To gain more robust statistics when investigating extreme events we create a lagged ensemble of eight
117 members. The ensemble is created by varying the initial times of the individual members. The sets of initial conditions are six hours
118 apart with the first member being initiated 2006-11-08 1800 UTC and the last one at 2006-11-11 0000 UTC. As mentioned above the
119 time period that is analyzed in this study is November 2006-11-11 1200 UTC - 2006-11-19 1200 UTC allowing for at least 12 hours
120 spin up phase for each ensemble member. Each simulation (ensemble member) is then run for the entire period, while the boundaries
121 of the 4 km domain is constrained by the ERA-I large-scale conditions. Although the simulations are long (more than eight days), it
122 will be shown that because of the localised forcing of these events later stages of the simulation still provide good representation of the
123 timing of the storms. Moreover, the outermost boundaries of the 4 km domain are also constrained by the reanalysis, which constrains
124 the large-scale conditions.

125 2.4. Thunderstorm Tracking

126 To investigate storm life cycles and their statistics of extreme events we track thunderstorm cells in observed and model data using
127 the TINT (Fridlind et al. 2019) storm tracking package. The cell tracks are retrieved using phase correlation between two consecutive
128 time steps and application of the Hungarian Maximum Matching Algorithm (Kuhn 1955) to identify cells that are connected in time.
129 We adopted the original package, that has been developed for radar data only, to be able to track model and radar based rainfall data
130 alike. For both the model and the radar, we apply a rain-rate threshold 0.1 mm/h and choose a minimum storm size 2 pixels to identify
131 storms. We will therefore refer to any contiguous rainfall region that gets identified by the tracking algorithm as a *storm*, regardless
132 of its intensity or duration. This also includes rainfall areas that are not the result of deep convection and that wouldn't necessarily be
133 called a thunderstorm.

134 3. Results

135 Before investigating the results of the experiment we focus on the large-scale atmospheric conditions over the study area during the
136 considered time period (Nov. 11 - 19 2006). These large-scale conditions are taken from the ERA-Interim reanalysis dataset. Mid-
137 tropospheric prevailing winds are easterly (Figure 2-a) advecting only moderately moist air into the domain (Figure 2-b). The mean
138 vertical motion is downward in the mid-troposphere (Figure 2-c), which along with the relatively dry profile, suppresses large-scale
139 convection. These properties are characteristic of the monsoon build up period described in Narsey et al. (2017).

140 3.1. Domain and Time Averages

141 After confirming that atmospheric conditions are favorable for locally forced convection we investigate how well averages of rainfall
 142 are captured by the model. Figure 3 compares time series of ensemble mean simulated rainfall with observations from the CPOL radar.
 143 Most of the Hector events, occurring in the afternoons, are captured by both model simulations (UM 1.33km and UM 0.44km). The
 144 simulated events during the afternoons of Nov. 13th, 14th and 15th are considerable weaker than the observations suggest. Around noon
 145 of the 17th of November an early rainfall peak occurs in the observations which is not captured by both sets of simulations. Though
 146 later that afternoon a second peak is represented well. Because of this three weaker and missed events the simulated mean rainfall is in
 147 both model simulations lower than in the observations though there are many days where there is reasonably good agreement between
 148 the observations and simulations, there are only some occasions where the model is too intense (e.g., 12 November). Overall there is
 149 reasonable agreement amongst the ensemble members; only towards the end of the simulation becomes the ensemble spread noticeable,
 150 which is perhaps expected due to the longer lead time. The dashed lines of Figure 3 represent the intensity of the 80th percentile of the
 151 area averaged rain-rates and show a decreased intensity of strong events (80+ percentiles) in the sub-km model simulations (0.44 km),
 152 but closer agreement between the 1.33 km model and the observations. The time series also reveals that the rainfall peaks in the model
 153 occur generally too early, except for the strong event in the afternoon of the 17th of November. Despite some of the differences in storm
 154 intensity and the above-mentioned missed event, the ensemble simulations produce a 'Hector' storm every day. This means that there
 155 is a total of 64 Hector events simulated for each model resolution, which is a good sample size for comparison between resolutions and
 156 to the observations.

157 The interpretation of domain average rainfall can be misleading when the occurrence of those rainfall events is spatially isolated. We
 158 therefore compare maps of time averages shown in Figure 4. The maps reveal spatial rainfall biases. While the observations suggest that
 159 rainfall is predominantly occurring over the south east the smaller Barthurst Island simulated rainfall occurs mainly over the centre of
 160 the large Melville Island. The ensemble standard deviation (centre row of Figure 4) shows maxima over Melville Island which indicates
 161 that most storms are confined to this area. As a consequence the simulated rainfall only exceeds the rain-rates of the observation in this
 162 area (bottom row of Figure 4). A slight decrease of rainfall bias in the sub-km simulation compared the km version can be noticed, yet
 163 both simulations do on average underestimate the mean intensity of rainfall in the study domain.

164 An important aspect of simulating tropical convection is the right timing. Previous studies have suggested that convection-permitting
 165 models (including the UM) trigger convection too early leading to biases in the diurnal rainfall cycle. We now investigate whether
 166 increasing to sub-km scales improves the representation of the diurnal cycle (Figure 5). Most notable is that in both simulations the
 167 ensemble average daily rainfall peak occurs roughly 2 hours earlier than the radar data peak. The early morning peak in the observations
 168 around 0300 - 0400 is also not captured in either sets of the model simulations. The occurrence timing of daily rainfall maximum per
 169 grid point is shown in Figure 5-a). The bias in the timing of the peak rainfall is likely related to the fact that (after the early morning
 170 observed peak) the rainfall initiates about an hour early in both model domains (approximately 1000 LT versus 1100 LT). Moreover,
 171 in the observations the rainfall continues to increase in magnitude until 1500 LT, potentially due to the development of stratiform
 172 rain, where the model rainfall decays earlier. The CPOL timing pattern suggests a propagation of storm systems from the north-east
 173 of Melville Island across the centre of the island in the afternoon towards the south flank of Barthurst Island. This propagation is not
 174 fully captured by both models. While there is some simulated propagation of convective systems from the north east of Melville island
 175 towards the centre around noon the convection remains concentrated over the centre of the island. This is consistent with with spatial
 176 occurrence of rainfall in Figure 4 where most of the rainfall is located over the centre of Melville island. It can be summarized that
 177 on average simulated rain-rates are slightly under estimated compared to observations. Model rain is mainly focused over the centre
 178 of Melville Island which differs from the observations where convection is propagating across both islands with peaks over Barthurst

179 Island. Compared to the CPOL observational data the simulated rainfall occurs too early. Some of these timing and magnitude errors
 180 may be related to a failure of the model to develop enough stratiform rain in the afternoon, a problem slightly more prevalent in the
 181 higher resolution model. These errors are consistent with the changes in storm characteristics identified in the next section.

182 *3.2. Storm track analysis*

183 Because the thunderstorms are isolated and the rainfall field is sparse in space and time conclusions drawn from averaging can be
 184 misleading. We now want avoid averaging as much as possible and look at individual storms while preserving statistical robustness.
 185 To do so we track individual storms in space and time using the tracking algorithm described in section 2-2.4. The reader is reminded
 186 here that we call any contiguous rainfall area that gets picked up by the tracking algorithm as a storm, regardless of its size or intensity.
 187 Here the storm size is measured as an equivalent radius, which is calculated from the median storm area. The number of storms for the
 188 model simulations is the ensemble average.

189 Table 1 summarizes the median properties of the identified storm tracks.

190 Most notable is the difference in storm size and number between model simulations and observations. The simulated storms are
 191 smaller in size but more numerous. The smallest and shortest storms occur in the sub-km model simulations. The UM 0.44km version
 192 also overestimates the storm intensities with an average rain-rate per storm of 5.65 mm/h. With 4.78 mm/h the 1.33km version only
 193 slightly overestimates the storm intensities, compared to its sub-km counterpart. This is in contrast to the results shown in Section 3-3.1
 194 where time and domain averaged rainfall is smaller in the simulations. This underestimation is most likely a result of a combination of
 195 decreased simulated storm areas (UM 1.33km) and shorter duration (UM 0.44km).

196 We now want to investigate storm properties of more extreme events and group storms by their rainfall intensity. To cater for the
 197 different intensities in model simulations and observations we group the storms by their rain-rate quintiles and compare the distributions
 198 of properties from individual storm cells within each quintile group. To average as little as possible and conserve a robust sample size
 199 when grouping the dataset we choose to consider individual storm cells rather taking averages of storm properties across their life-
 200 cycles. Figure 6 shows distributions of the three storm cell properties rain-rate, duration and size (equivalent radius) grouped by
 201 rain intensity (quintiles). The rain-rates for both simulated and observed storms are increasing with quintile as expected. They are
 202 considerably higher in the sub-km model simulations than its 1.33 km counterpart which, in turn are higher across all quintiles than
 203 the observations. With increasing quintile the gap between observations and model simulations becomes larger. The pattern of storm
 204 duration and size with increasing rain intensity also reflects the results shown in Table 1. The sub-km model storms have a shorter
 205 duration and a smaller size than 1.33 km model and the observed storms too. It is interesting to note that there is only a moderate
 206 increase in storm duration with quintiles for simulations and observation alike. This is also the case for the storm sizes, except for the
 207 UM 1.33km model version, where a jump in duration can be observed between the 3rd and 4th quintile. This jump contributes to the
 208 decreased size bias of the 1.33km version shown in Table 1.

209 Figure 4 suggests that the majority of the simulated storms do develop and disappear over the centre of Melville island while
 210 propagation across both Tiwi Islands is observed. This can easily be confirmed with help of the storm track analysis. Figure 7 displays
 211 tracks for the most intense storms (5th quintile). Most of the simulated tracks are concentrated over the centre of Melville Island. This
 212 is in stark contrast to the observed storm tracks which are all propagating from east to west across the Tiwis. The track length of
 213 simulated storms is also much shorter than for the observed storms. Although most of the simulated storms do propagate from east to
 214 west (• indicates initiation of the storm and ∗ its decay) some storms propagate into the opposite direction. As shown here for the most
 215 intense quintile the sub-km model version produces overall more numerous and shorter storms than the 1.33 km model, which is also
 216 the case for the fourth quintile.

At this point it can be summarized that the simulated storms are smaller in size, more numerous and more intense than the observed storms. Most of the intense storms are confined to a rather small area over the centre of Melville Island. This is contrast to the observations that show systems propagating across the Tiwi Islands. The increased number of storms and intensity can not fully compensate for the effects of decreased size and life time in the case of the sub-km model version. The detailed storm track investigation suggested that increasing the resolution to sub-km scales does not necessarily lead to a better representation of storms and by some measures the characteristics of the more intense storms are worse.

223 3.3. Convection and cold pool properties

224 We now want to answer the question of why the sub-km model version is performing poorer than its km-scale counterpart and
 225 investigate atmospheric conditions in which the simulated storms occur. Because we do not have adequate observations of the meso-
 226 scale structure of the atmosphere this section only considers the two model versions and not the observations.

227 Making statements about simulated atmospheric conditions that are associated with thunderstorms is somewhat tricky. One approach
 228 might be taking snap shots of the storm and investigate profiles of certain variables like vertical motion or moisture flux. We do not
 229 choose to take this approach as we want to take all simulated storms into account which allows for a more robust investigation of
 230 extreme events. Instead, we take the storms tracks and examine various atmospheric variables within individual storms along their
 231 trajectory. For simplicity we take the storm cell size s_{it} of a storm U_{it} at time t and estimate the vertical profile of the atmosphere
 232 within a square of size s_{it} at time t around the centre of U_{it} . This technique allows us to retrieve profiles for all individual storms cells
 233 in the dataset and to discriminate against storm cells with different intensities.

234 One important indicator of convection is the profile of vertical motion anomalies $\bar{w}' = \langle w - \bar{w} \rangle$. Where \bar{w} is computed from the
 235 domain averaged vertical velocity at a given model level. Figure 8-a) shows the average profile of vertical motion grouped by storm
 236 intensity. Overall a strong increase in mean updraft strength with storm intensity can be noticed. This is as expected since the considered
 237 storms are of convective nature and there is a close association between rain rate (used to define the quintiles) and updraft strength.
 238 The less intense storms, within 1st and 2nd quintiles, are associated with vertical motion that is peaking the lower troposphere, which
 239 indicates that the associated convection is not deep and is mainly in the boundary layer or congestus. The more intense storms are not
 240 surprisingly associated with vertical motion profiles found in deeper convective system where an intensification of vertical motion in the
 241 mid-troposphere can be observed. The differences of the two profiles for 1.33 km and 0.44 km model is noteworthy. This is especially
 242 true of the upper quintile, where the 1.33 and 0.44 km models possess different shapes to the profile; the 1.33 km model has a peak
 243 in the upper-troposphere. Figure 8-b) displays the average profiles of turbulent moisture flux, which are closely linked to the vertical
 244 motion profiles. Peaks over vertical moisture fluxes occur in the upper-mid troposphere for the the highest percentiles. The differences
 245 of the flux and vertical moisture profiles between the two model simulations are consistent with the behavior of rainfall in Figure 6. For
 246 the upper three quintiles, the 1.33 km model shows fluxes extending deeper than the 0.44 km model. Such deeper updraft effects would
 247 be consistent with reduced entrainment in the coarser model as suggested by [Bryan et al. \(2003\)](#). The fluxes are, however, stronger in
 248 the higher resolution model (for the upper two quintiles), conferring with Figure 6-b this suggests that as the storms are shorter-lived
 249 they must become more intense. These results have some consistency with [Jucker et al. \(2020\)](#), who showed a strengthening of the
 250 kinetic energy spectrum for the smallest resolvable scales. Such a strengthening would lead to the smaller, stronger storm cells shown
 251 here, suggesting ineffective mixing and a dominance of numerical effects on these scales. An important model component that can
 252 modify the characteristics of convection and subsequently rainfall is the cloud micro-physics. To consider this, the average liquid water
 253 and graupel content per storm is displayed in Figure 8-d. The profiles of liquid water content, q_l , follow a similar pattern to the vertical
 254 velocity, with the 1.33 km model being stronger at lower quintiles and the 0.44 km model being stronger at upper quintiles. For the
 255 graupel, however, it is only the 4th and 5th quintiles that show the large increase in graupel in the 0.44 km model. These results suggest

256 that the strongest storms in the 0.44 km model are much more effective in transporting moisture to the upper-troposphere, with the
 257 formation of graupel being one consequence. These changes in microphysical properties between the 1.33 and 0.44 km storms likely
 258 have important feedbacks on rainfall, evaporation and other storm properties.

259 As mentioned in section 1 due to the topographic setup of the Tiwi Islands, thunderstorm events can intensify by interaction of
 260 sea-breeze convergence lines and outflows from the convective systems. This suggests that the boundary layer can play an important
 261 role for the intensification of the storms, especially via cold-pools. To find any relationships of the tracked storms and cold-pool fields
 262 we first calculate the perturbations of surface density potential temperature (θ_p). Here we follow the approach of Tompkins (2001) and
 263 define θ_p at the surface as:

$$\theta_p = \theta \cdot (1 + 0.608 \cdot r_v - r_r) \quad (1)$$

264 with θ being the potential temperature and $r_{v/r}$ the mixing ratios for water vapor and rain. We follow the procedure mentioned above
 265 and retrieve the perturbation field of θ_p for each identified storm and group the $\overline{\theta_p'}$ values by storm intensity (Figure 9-a).

266 Overall there is only a weak θ_p decrease with storm intensity, which is more discernible for the sub-km version, to be recognized.
 267 For the weak storms the medians of the distributions are positive or only slightly negative which indicates either the absences or very
 268 moderate density perturbations. With increasing storm intensity the θ_p perturbation for the sub-km model decrease slightly. The inter
 269 model comparison suggests that there might be a small intensification of cold-pool activity in the sub-km scale model, for quintiles 4
 270 and 5, consistent with the stronger rain rates seen earlier.

271 The above comparison of density potential temperature, as a function of storm intensity does not show a clear signal. To gain deeper
 272 insights on cold pool strength in the two simulations we utilize the perturbation fields of θ_p and apply a threshold of 0 K to track
 273 cold-pools using the tracking algorithm introduced above. We do not choose to compare the cold-pool tracks with the storm tracking
 274 results here as matching storms tracks to cold pool tracks have many ambiguities, especially in region with multiple storms and cold
 275 pools. Figure 10 compares the probability density functions of tracked cold-pools, represented by θ_p anomalies, for the two model
 276 simulations. The two distributions show a clear bi-modal behavior, where the second mode that is associated with stronger cold pools
 277 has higher densities in the sub-km ensemble simulations. As a consequence the cold pools in the 0.44 km models are -0.71 K on
 278 average (13.15 %), stronger than in the 1.33 km version (-0.66 K), as discussed above stronger cold pools are consistent with the more
 279 intense rain for the 0.44 km model.

280 4. Summary and Discussion

281 This study investigated the representation of intense convective rainfall events in a set of simulations using km and sub-km scale grid
 282 spacings. We focused on the simulation of a sequence of island thunderstorm events over the Tiwi Islands in Northern Australia during
 283 the build up period of the Australian Summer Monsoon in November 2006. We chose the build up period as the convection is mainly
 284 locally forced which reduces (but does not eliminate) the effect of the global input model and variations in the larger scale forcing.
 285 The model setup uses ERA-Interim reanalysis data as initial and boundary conditions for a nested setup with horizontal grid spacings
 286 equal to 4 km, 1.33 km and 0.44 km. Our particular focus was on the more intense events within the two finest grids with grid spacing
 287 equal to 1.33 and 0.44 km. To increase the sample size which can be low for intense events we chose to create an ensemble of eight
 288 members; with our focus on an eight day period, the model ensemble therefore produced 64 daily storm events (viz. 'Hectors').

289 Applying spatial and temporal averaging suggested that both model resolutions underestimate the rain-rates when compared to
 290 observations. This is in part due to three strong rainfall events that are missed by the model simulations (Figure 3). The geo-spatial
 291 distribution of rainfall (Figure 4) showed that simulated rainfall is concentrated over the centre of the Tiwi's main island while rainfall
 292 peaks in the observations are mainly occurring in the east and west of the domain. An investigation of the timing of convection

293 confirmed results of other studies using high resolution simulation: on average the simulated rainfall peak occurs too early. Increasing
 294 the resolution slightly worsened the rainfall timing. By only considering spatio-temporal averages of rainfall fields it can be summarized
 295 that the intensity of island thunderstorm events are underestimated by the model and increasing the resolution to sub-km scales does
 296 not significantly improve their representation. Although the errors in timing are consistent with recent studies of convection in the
 297 Maritime Continent using convection-permitting models (e.g [Vincent and Lane 2017; Jucker et al. 2020](#)), the errors in amplitude are
 298 different. The main difference between [Jucker et al. \(2020\)](#), who showed the modelled rainfall over the mainland to be too intense, and
 299 the results herein is that the convection over the islands here does not become organised and is mostly comprised of short-lived cells.
 300 The reasons for these differences should be a topic of future research.

301 To get more meaningful insights of single events while retaining statistical robustness we tracked observed and simulated storm
 302 events in space and time by objectively identifying storm objects. This allowed us to discriminate storm properties like size and
 303 duration against storm intensities. This comparison showed that simulated thunderstorm events are in general more numerous, smaller
 304 and intense. The underestimation of area/time averaged rain-rates is hence the result of a combination of smaller, slightly shorter
 305 lived storms that are focused over a comparable small area and that are more intense. It is noteworthy that increasing the resolution
 306 worsens this effect, storms in the sub-km model are even shorter, smaller and more intense than observed, especially for the strongest
 307 storms. This result is in contrast to some previous studies, which suggest that at sub-km scales the increase in resolved entrainment
 308 should weaken updrafts ([Bryan et al. 2003](#)). However, the result is consistent with tendency for this specific model to have enhanced
 309 kinetic energy at the smallest resolvable scales ([Jucker et al. 2020](#)), which leads to intense and small updrafts. A clear increase of
 310 mid-tropospheric turbulent vertical velocity and moisture flux in the sub-km model is the reason for this intensification of storms. The
 311 comparison of graupel content exhibits decreased graupel contents in the sub-km version, likely related to the smaller and shorter-lived
 312 storms.

313 We also examined any changes in cold pool intensity with resolution by applying the above mentioned tracking algorithm to
 314 perturbation fields of density potential temperature. The results of this tracking do confirm that cold pools in the sub-km models are
 315 more intense. This increased cold pool intensity may be a result of the stronger rainfall in the sub-km model, but may also contribute
 316 to an increase in rainfall intensity.

317 The question of cold pool activity is also very important to answer as previous studies suggested that an interaction of sea-breeze
 318 fronts and cold air outflow from developing convection play an important role in the intensification and formation of extreme island
 319 thunderstorm systems. A feedback sequence of how simulated storms intensify could be described as follows:

- 320 1. Low level sea-breeze convergence causes occurrence of convection which is focused on a rather small area.
- 321 2. This convection also causes water vapor to transform to liquid water which is then being transformed into ice, snow and graupel
 322 in upper part of the simulated cloud.
- 323 3. Evaporation of associated rain fluxes creates/intensifies cold pool in the boundary layer below the clouds.
- 324 4. Cold-pools produce stronger convergence by interaction with the sea-breeze fronts and/or cold air outflow from neighboring
 325 clouds.

326 According to the above mentioned sequence, shortcomings in the micro-physics parametrization could cause feedback loops, with
 327 more intense updrafts as a result. This final point highlights the importance of physical parameterizations, such as microphysics and
 328 turbulence, and their role in contributing to resolution sensitivities. Complex NWP-style models, such as the Unified model, make
 329 disentangling the causes of resolution sensitivity challenging and changes to one scheme have downstream influences on others. To
 330 fully test the above outlined possible mechanism we suggest that future studies should aim to investigate the impact of physical
 331 parameterizations, especially at sub-km scales, with simpler model frameworks. We recognise that there are many such idealized

332 studies in the literature already, but it appears that some of these resolution sensitivities are model specific (e.g Jucker et al. 2020),
 333 making such idealized studies with the Unified model necessary. Emphasise should be given to tuning parameters which have to be set
 334 manually - deep learning algorithms are well suited for optimizing large sets of tuning parameters. Investigating the capabilities of such
 335 machine learning tools might be a step towards significant improvements of remaining parametrizations in high resolution numerical
 336 weather prediction and climate models.

337 Acknowledgement

338 This work was funded by the Australian Research Council's (ARC) Centre of Excellence for Climate Extremes (CLEX, grant number
 339 : CE170100023) Observations from the CPOL Doppler Radar have been made available by the Bureau of Meteorology. The tracking
 340 algorithm is published under MIT open source license and can be retrieved via <https://zenodo.org/record/3250273>.
 341 Computing facilities were provided by the National Computational Infrastructure (NCI) facility in Canberra, Australia. Thank you to
 342 Stuart Webster, UK Met Office, for assistance with the model.

343 References

- 344 Bergemann, M., and C. Jakob, 2016: How important is tropospheric humidity for coastal rainfall in the tropics? *Geophysical Research Letters*, **43** (19), 5860–
 345 5868, 2016GL069255.
- 346 Bergemann, M., C. Jakob, and T. P. Lane, 2015: Global detection and analysis of coastline-associated rainfall using an objective pattern recognition technique.
 347 *Journal of Climate*, **28** (18), 7225–7236.
- 348 Beringer, J., N. J. Tapper, and T. D. Keenan, 2001: Evolution of maritime continent thunderstorms under varying meteorological conditions over the tiwi islands.
 349 *International Journal of Climatology*, **21** (8), 1021–1036, doi:10.1002/joc.622, <https://rmets.onlinelibrary.wiley.com/doi/10.1002/joc.622>.
- 350 Berrisford, P., and Coauthors, 2011: The era-interim archive version 2.0. Tech. rep., Shinfield Park, Reading, – pp.
- 351 Birch, C. E., S. Webster, S. C. Peatman, D. J. Parker, A. J. Matthews, Y. Li, and M. E. E. Hassim, 2016: Scale interactions between the mjo and the western
 352 maritime continent. *Journal of Climate*, **29** (7), 2471–2492, <http://dx.doi.org/10.1175/JCLI-D-15-0557.1>.
- 353 Boutle, I. A., J. E. J. Eyre, and A. P. Lock, 2014: Seamless stratocumulus simulation across the turbulent gray zone. *Mon. Wea. Rev.*, **142** (4), 1655–1668,
 354 doi:10.1175/MWR-D-13-00229.1.
- 355 Bryan, G. H., J. C. Wyngaard, and J. M. Fritsch, 2003: Resolution requirements for the simulation of deep moist convection. *Monthly Weather Review*, **131** (10),
 356 2394 – 2416, doi:10.1175/1520-0493(2003)131<2394:RRFTSO>2.0.CO;2, URL https://journals.ametsoc.org/view/journals/mwre/131/10/1520-0493_2003_131_2394_rrftso_2.0.co_2.xml.
- 358 Bush, M., and Coauthors, 2019: The first met office unified model/jules regional atmosphere and land configuration, ral1. *Geoscientific Model Development -
 359 Discussions*, **130**, doi:10.5194/gmd-2019-130.
- 360 Chan, S. C., E. J. Kendon, H. J. Fowler, S. Blenkinsop, C. A. T. Ferro, and D. B. Stephenson, 2013: Does increasing the spatial resolution of a regional climate
 361 model improve the simulated daily precipitation? *Climate Dynamics*, **41** (5), 1475–1495, URL <https://doi.org/10.1007/s00382-012-1568-9>.
- 362 Chan, S. C., E. J. Kendon, H. J. Fowler, S. Blenkinsop, N. M. Roberts, and C. A. T. Ferro, 2014: The value of high-resolution met office regional
 363 climate models in the simulation of multihourly precipitation extremes. *J. Climate*, **27** (16), 6155–6174, doi:10.1175/JCLI-D-13-00723.1, URL <https://doi.org/10.1175/JCLI-D-13-00723.1>.
- 365 Crook, N. A., 2001: Understanding hector: The dynamics of island thunderstorms. *Monthly Weather Review*, **129** (6), 1550–1563, doi:10.1175/1520-0493(2001)
 366 129<1550:UHTDOI>2.0.CO;2, [https://doi.org/10.1175/1520-0493\(2001\)129<1550:UHTDOI>2.0.CO;2](https://doi.org/10.1175/1520-0493(2001)129<1550:UHTDOI>2.0.CO;2).
- 367 Dauhut, T., J.-P. Chaboureau, J. Escobar, and P. Mascart, 2016: Giga-les of hector the convector and its two tallest updrafts up to the stratosphere. *Journal of the
 368 Atmospheric Sciences*, **73** (12), 5041–5060, doi:10.1175/JAS-D-16-0083.1, <https://doi.org/10.1175/JAS-D-16-0083.1>.
- 369 Dauhut, T., J.-P. Chaboureau, P. Mascart, and O. Pauluis, 2017: The atmospheric overturning induced by hector the convector. *Journal of the Atmospheric
 370 Sciences*, **74** (10), 3271–3284, doi:10.1175/JAS-D-17-0035.1, <https://doi.org/10.1175/JAS-D-17-0035.1>.
- 371 Dipankar, A., and Coauthors, 2020: Singy: A convective-scale weather forecast model for singapore. *Quarterly Journal of the Royal Meteorological Society*,
 372 **146** (733), 4131–4146, doi:<https://doi.org/10.1002/qj.3895>, URL <https://rmets.onlinelibrary.wiley.com/doi/abs/10.1002/qj.3895>, <https://rmets.onlinelibrary.wiley.com/doi/pdf/10.1002/qj.3895>.

- 374 Fridlind, A. M., and Coauthors, 2019: Use of polarimetric radar measurements to constrain simulated convective cell evolution: a pilot study with lagrangian
375 tracking. *Atmospheric Measurement Techniques*, **12** (6), 2979–3000, doi:10.5194/amt-12-2979-2019.
- 376 Gevorgyan, A., 2018: Convection-permitting simulation of a heavy rainfall event in armenia using the wrf model. *J. Geophys. Res. Atmos.*, **123** (19), 11,008–
377 11,029, doi:10.1029/2017JD028247, URL <https://doi.org/10.1029/2017JD028247>.
- 378 Gianotti, R. L., D. Zhang, and E. A. B. Eltahir, 2011: Assessment of the regional climate model version 3 over the maritime continent using different cumulus
379 parameterization and land surface schemes. *J. Climate*, **25** (2), 638–656.
- 380 Gill, A. E., 1980: Some simple solutions for heat-induced tropical circulation. *Quarterly Journal of the Royal Meteorological Society*, **106** (449), 447–462.
- 381 Hassim, M. E. E., T. P. Lane, and W. W. Grabowski, 2016: The diurnal cycle of rainfall over new guinea in convection-permitting wrf simulations. *Atmospheric
382 Chemistry and Physics*, **16** (1), 161–175.
- 383 Jucker, M., T. P. Lane, C. L. Vincent, S. Webster, S. A. Wales, and V. Louf, 2020: Locally forced convection in subkilometre-scale simulations with
384 the unified model and wrf. *Quarterly Journal of the Royal Meteorological Society*, **146** (732), 3450–3465, doi:<https://doi.org/10.1002/qj.3855>, URL
385 <https://rmets.onlinelibrary.wiley.com/doi/abs/10.1002/qj.3855>, <https://rmets.onlinelibrary.wiley.com/doi/pdf/10.1002/qj.3855>.
- 386 Keat, W. J., and Coauthors, 2019: Convective initiation and storm life cycles in convection-permitting simulations of the met office unified model over south
387 africa. *Q.J.R. Meteorol. Soc.*, **145** (721), 1323–1336, doi:10.1002/qj.3487.
- 388 Keenan, T., K. Glasson, F. Cummings, T. S. Bird, J. Keeler, and J. Lutz, 1998: The bmrc/near c-band polarimetric (c-pol) radar system. *J. Atmos. Oceanic
389 Technol.*, **15** (4), 871–886, doi:10.1175/1520-0426(1998)015<0871:TBNCBP>2.0.CO;2.
- 390 Keenan, T., and Coauthors, 2000: The maritime continent – thunderstorm experiment (mctex): Overview and some results. *Bull. Amer. Meteor. Soc.*, **81** (10),
391 2433–2456, doi:10.1175/1520-0477(2000)081<2433:TMCTEM>2.3.CO;2.
- 392 Keenan, T. D., B. R. Morton, M. J. Manton, and G. J. Holland, 1989: The island thunderstorm experiment (itex)—a study of tropical thunderstorms in the
393 maritime continent. *Bull. Amer. Meteor. Soc.*, **70** (2), 152–159, doi:10.1175/1520-0477(1989)070<0152:TITESO>2.0.CO;2.
- 394 Kuhn, H. W., 1955: The hungarian method for the assignment problem. *Naval Research Logistics Quarterly*, **2** (1-2), 83–97, doi:<https://doi.org/10.1002/nav.3800020109>, URL <https://onlinelibrary.wiley.com/doi/abs/10.1002/nav.3800020109>, <https://onlinelibrary.wiley.com/doi/pdf/10.1002/nav.3800020109>.
- 395 Leroy, D., and Coauthors, 2016: Haic/hiwc field campaigns - specific findings on ice crystals characteristics in high ice water content cloud regions. *AIAA
396 AVIATION Forum*, American Institute of Aeronautics and Astronautics, –, doi:10.2514/6.2016-4056.
- 397 Louf, V., A. Protat, R. A. Warren, S. M. Collis, D. B. Wolff, S. Rauniar, C. Jakob, and W. A. Petersen, 2018: An integrated approach to weather radar calibration
398 and monitoring using ground clutter and satellite comparisons. *J. Atmos. Oceanic Technol.*, **36** (1), 17–39, doi:10.1175/JTECH-D-18-0007.1.
- 399 Love, B. S., A. J. Matthews, and G. M. S. Lister, 2011: The diurnal cycle of precipitation over the maritime continent in a high-resolution atmospheric model.
400 *Q.J.R. Meteorol. Soc.*, **137** (657), 934–947, doi:10.1002/qj.809.
- 401 Matsuno, T., 1966: Quasi-geostrophic motions in the equatorial area. *J. Meteor. Soc. Japan*, **44** (1), 25–43.
- 402 May, P. T., J. H. Mather, G. Vaughan, C. Jakob, G. M. McFarquhar, K. N. Bower, and G. G. Mace, 2008: The tropical warm pool international cloud experiment.
403 *Bull. Amer. Meteor. Soc.*, **89** (5), 629–646, doi:10.1175/BAMS-89-5-629.
- 404 Mori, S., and Coauthors, 2004: Diurnal land-sea rainfall peak migration over sumatera island, indonesian maritime continent, observed by trmm satellite and
405 intensive rawinsonde soundings. *Mon. Wea. Rev.*, **132** (8), 2021–2039.
- 406 Narsey, S., M. J. Reeder, D. Ackerley, and C. Jakob, 2017: A midlatitude influence on australian monsoon bursts. *J. Climate*, **30** (14), 5377–5393, doi:
407 10.1175/JCLI-D-16-0686.1.
- 408 Qian, J.-H., 2008: Why precipitation is mostly concentrated over islands in the maritime continent. *J. Atmos. Sci.*, **65** (4), 1428–1441.
- 409 Ramage, C. S., 1968: Role of a tropical “maritime continent” in the atmospheric circulation. *Monthly Weather Review*, **96** (6), 365–370.
- 410 Saito, K., T. Keenan, G. Holland, and K. Puri, 2001: Numerical simulation of the diurnal evolution of tropical island convection over the maritime continent.
411 *Mon. Wea. Rev.*, **129** (3), 378–400, doi:10.1175/1520-0493(2001)129<0378:NSOTDE>2.0.CO;2.
- 412 Schafer, R., P. T. May, T. D. Keenan, K. McGuffie, W. L. Ecklund, P. E. Johnston, and K. S. Gage, 2001: Boundary layer development over a tropical island
413 during the maritime continent thunderstorm experiment. *Journal of the Atmospheric Sciences*, **58** (15), 2163–2179, doi:10.1175/1520-0469(2001)058<2163:
414 BLDOAT>2.0.CO;2, [https://doi.org/10.1175/1520-0469\(2001\)058<2163:BLDOAT>2.0.CO;2](https://doi.org/10.1175/1520-0469(2001)058<2163:BLDOAT>2.0.CO;2).
- 415 Simpson, J., T. Keenan, B. Ferrier, R. Simpson, and G. Holland, 1993: Cumulus mergers in the maritime continent region. *Meteorology and Atmospheric
416 Physics*, **51** (1-2), 73–99.
- 417 Simpson, J., N. Westcott, R. Clerman, and R. Pielke, 1980: On cumulus mergers. *Archiv für Meteorologie, Geophysik und Bioklimatologie, Serie A*, **29** (1-2),
418 1–40.

- 420 Thompson, E. J., S. A. Rutledge, B. Dolan, M. Thurai, and V. Chandrasekar, 2017: Dual-polarization radar rainfall estimation over tropical oceans. *J. Appl. Meteor. Climatol.*, **57** (3), 755–775, doi:10.1175/JAMC-D-17-0160.1.
- 421 Tompkins, A. M., 2001: Organization of tropical convection in low vertical wind shears: The role of cold pools. *J. Atmos. Sci.*, **58** (13), 1650–1672, doi:10.1175/1520-0469(2001)058<1650:OOTCIL>2.0.CO;2.
- 422 Trenberth, K. E., J. T. Fasullo, and J. Kiehl, 2009: Earth's global energy budget. *Bull. Amer. Meteor. Soc.*, **90** (3), 311–324, doi:10.1175/2008BAMS2634.1.
- 423 Vaughan, G., C. Schiller, A. R. MacKenzie, K. Bower, T. Peter, H. Schlager, N. R. P. Harris, and P. T. May, 2008: Scout-o3/active: High-altitude aircraft measurements around deep tropical convection. *Bull. Amer. Meteor. Soc.*, **89** (5), 647–662, doi:10.1175/BAMS-89-5-647.
- 424 Vincent, C. L., and T. P. Lane, 2017: A 10-year austral summer climatology of observed and modeled intraseasonal, mesoscale, and diurnal variations over the maritime continent. *Journal of Climate*, **30** (10), 3807 – 3828, doi:10.1175/JCLI-D-16-0688.1, URL <https://journals.ametsoc.org/view/journals/clim/30/10/jcli-d-16-0688.1.xml>.
- 425 Wilson, D. R., and S. P. Ballard, 1999: A microphysically based precipitation scheme for the uk meteorological office unified model. *Quarterly Journal of the Royal Meteorological Society*, **125** (557), 1607–1636, doi:10.1002/qj.49712555707, <https://rmets.onlinelibrary.wiley.com/doi/pdf/10.1002/qj.49712555707>.
- 426 Wilson, D. R., A. C. Bushell, A. M. Kerr-Munslow, J. D. Price, and C. J. Morcrette, 2008: Pc2: A prognostic cloud fraction and condensation scheme. i: Scheme description. *Q.J.R. Meteorol. Soc.*, **134** (637), 2093–2107, doi:10.1002/qj.333.
- 427 Yamanaka, M. D., S.-Y. Ogino, P.-M. Wu, H. Jun-Ichi, S. Mori, J. Matsumoto, and F. Syamsudin, 2018: Maritime continent coastlines controlling earth's climate. *Progress in Earth and Planetary Science*, **5** (1), 21–, doi:10.1186/s40645-018-0174-9.
- 428 Zhu, M., P. Connolly, G. Vaughan, T. Choularton, and P. T. May, 2012: Numerical simulation of tropical island thunderstorms (hectors) during the active campaign. *Meteorological Applications*, **20** (3), 357–370, doi:10.1002/met.1295, <https://rmets.onlinelibrary.wiley.com/doi/pdf/10.1002/met.1295>.

438 **List of Tables**

	UM 1.33km	UM 0.44km	CPOL
Equiv. Radius [km]	4.94	4.42	5.94
Duration [min]	60.00	50.00	60.00
Avg. rain-rate [mm/h]	4.78	5.65	4.52
Max. rain-rate [mm/h]	6.90	8.56	6.79
Speed [km/h]	10.03	12.71	12.67
# Storms	73	50	42

Table 1. Median properties of objectively tracked storms. The storm count (# Storms) is given as an ensemble average for the simulated data (UM 1.33km and UM 0.44km)

439 List of Figures

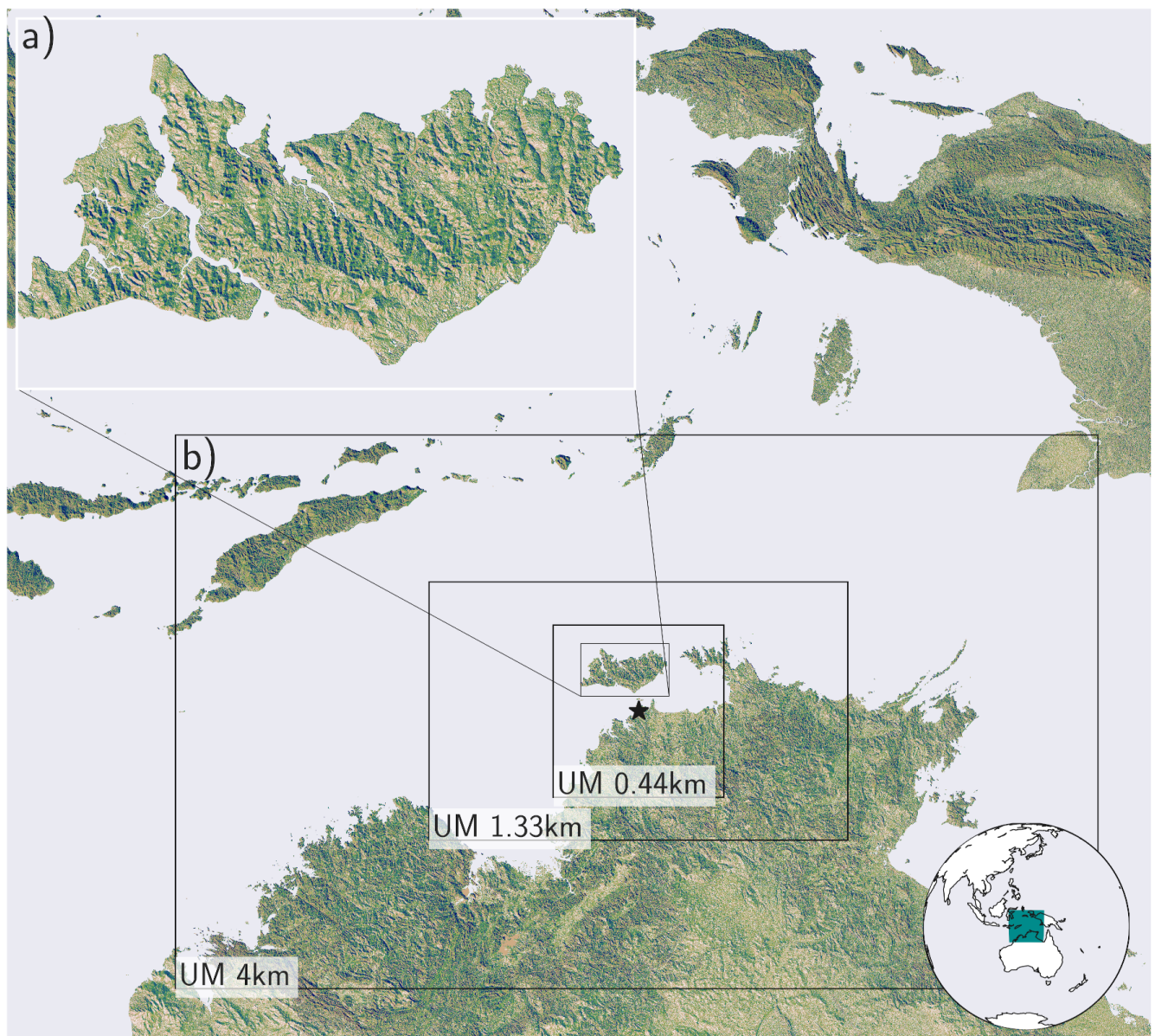


Figure 1. The Tiwi Islands study domain (a). The model domain boundaries of the triple nested setup with their horizontal resolution is shown in b). The location of the CPOL radar station is indicated by a black star.

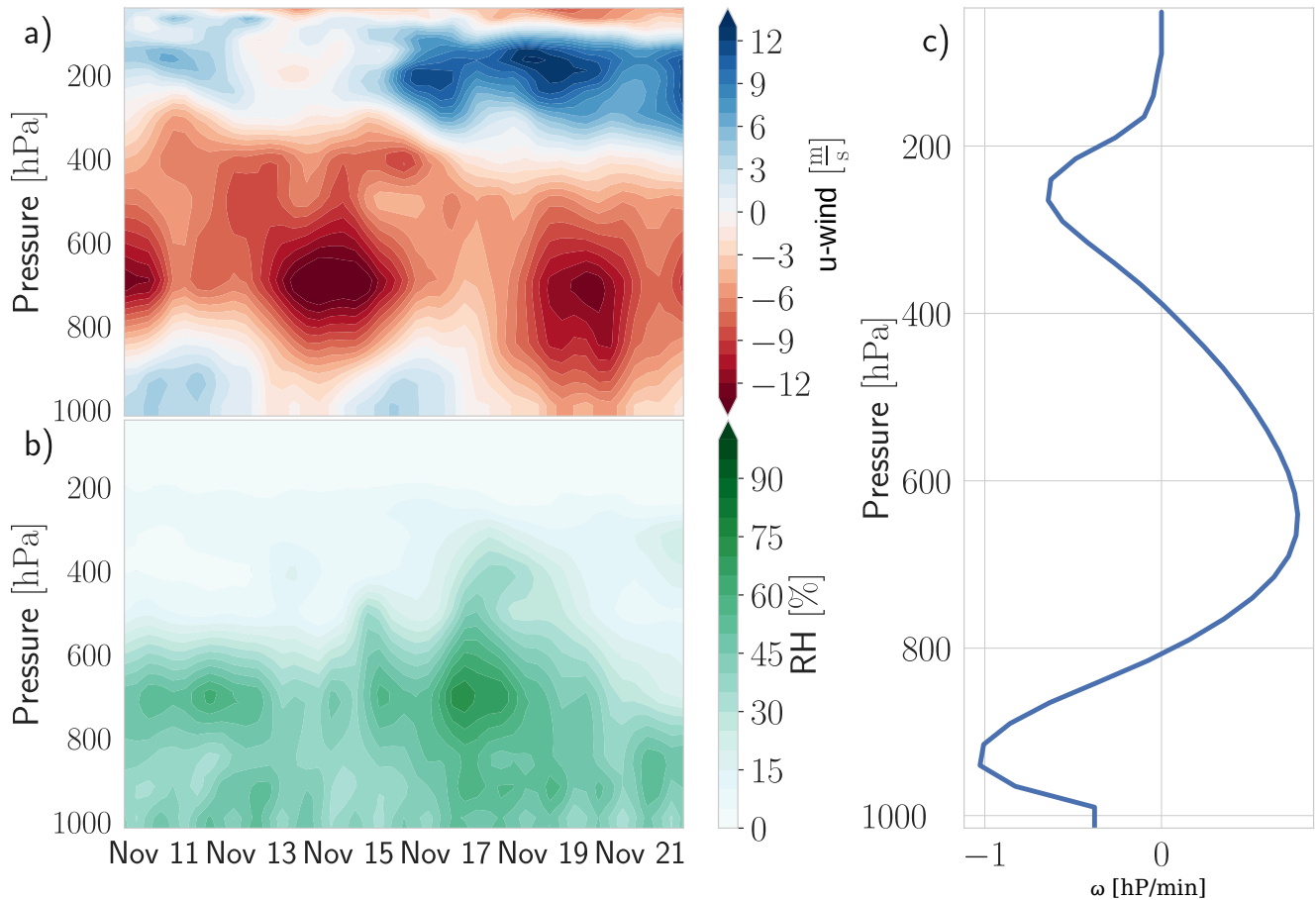


Figure 2. Large-Scale atmospheric conditions between Nov. 11 and Nov. 19 2006 over the study domain. a) u-component of horizontal winds, b) relative humidity and c) average vertical ω profile.

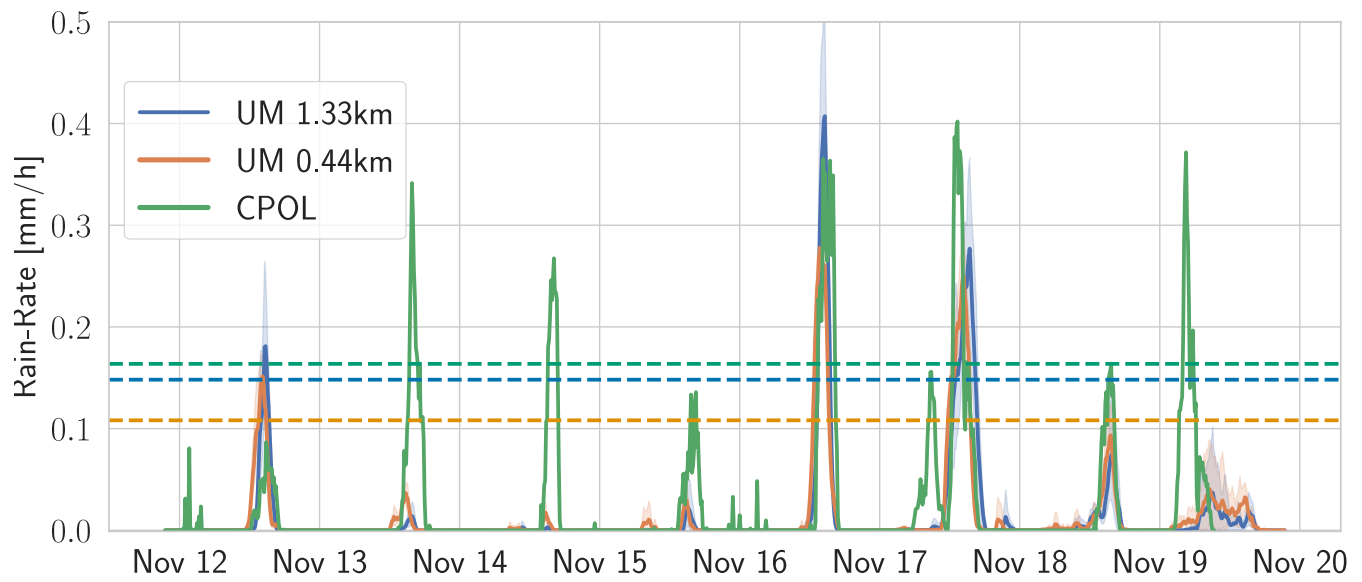


Figure 3. Rainfall: domain averages of simulated ensemble means compared with observations. The individual ensemble members are indicated by the shading. Dashed lines indicate the 80th percentile of field averaged rain-rates.

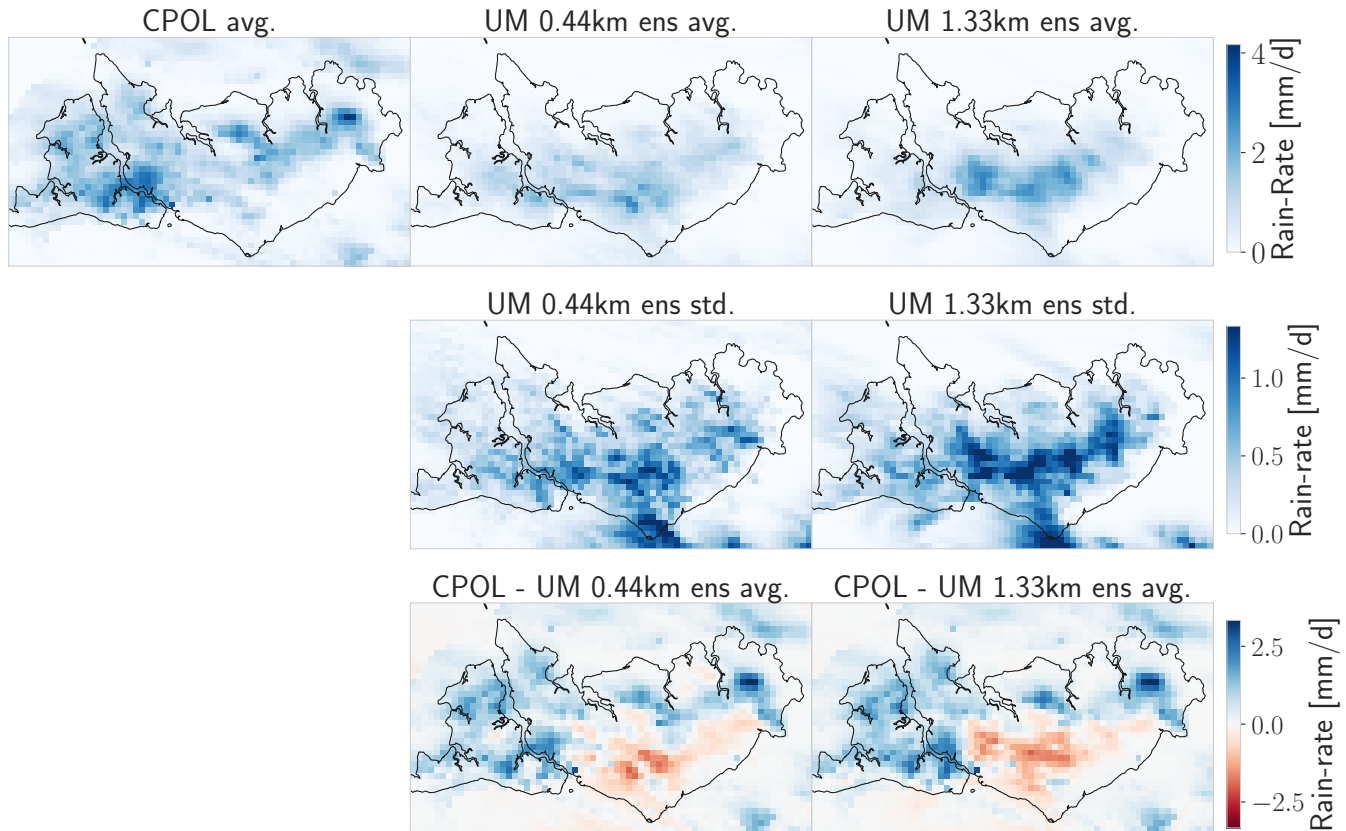


Figure 4. Maps of time averaged rain-rates (mm/d). The top row shows the observations (CPOL) along with ensemble averages of the 0.44 km and 1.33 km simulations. The centre row represents the ensemble standard deviation of both model simulations while the bottom row indicates the difference of the simulated ensemble mean and the observations.

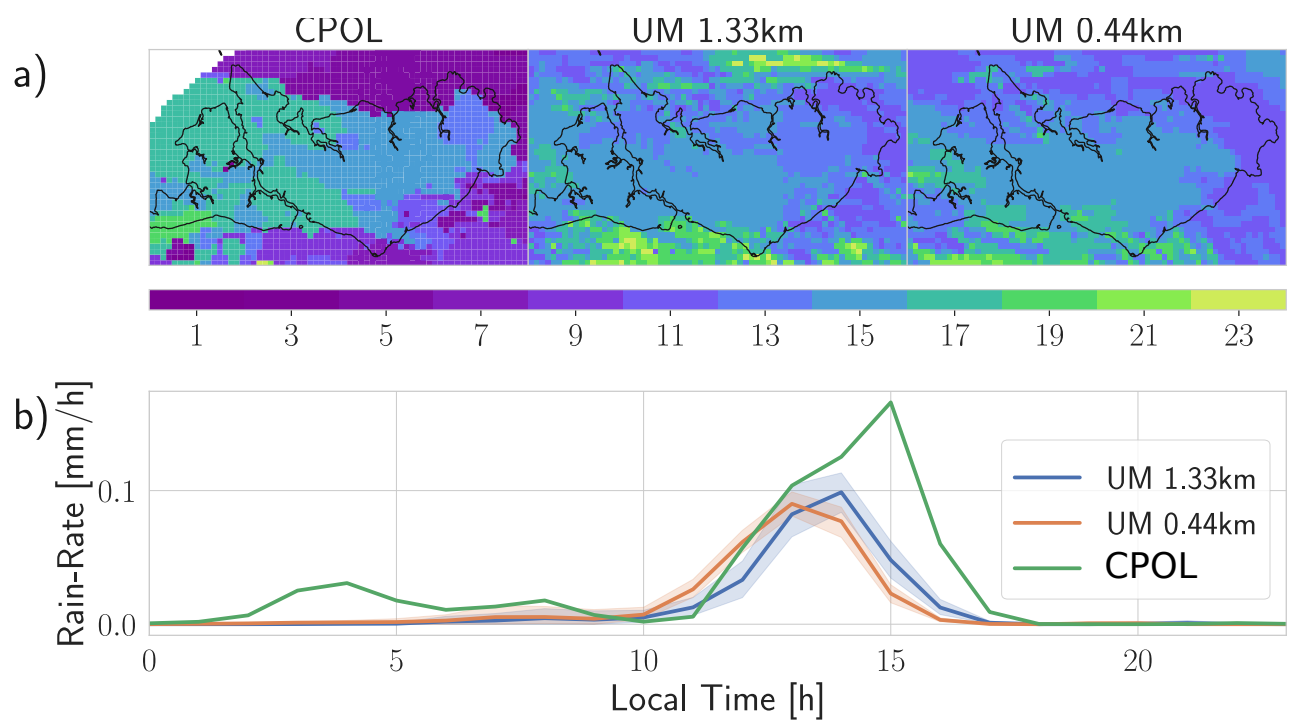


Figure 5. a) Map of timing of daily rainfall peaks. b) Domain average diurnal cycle.

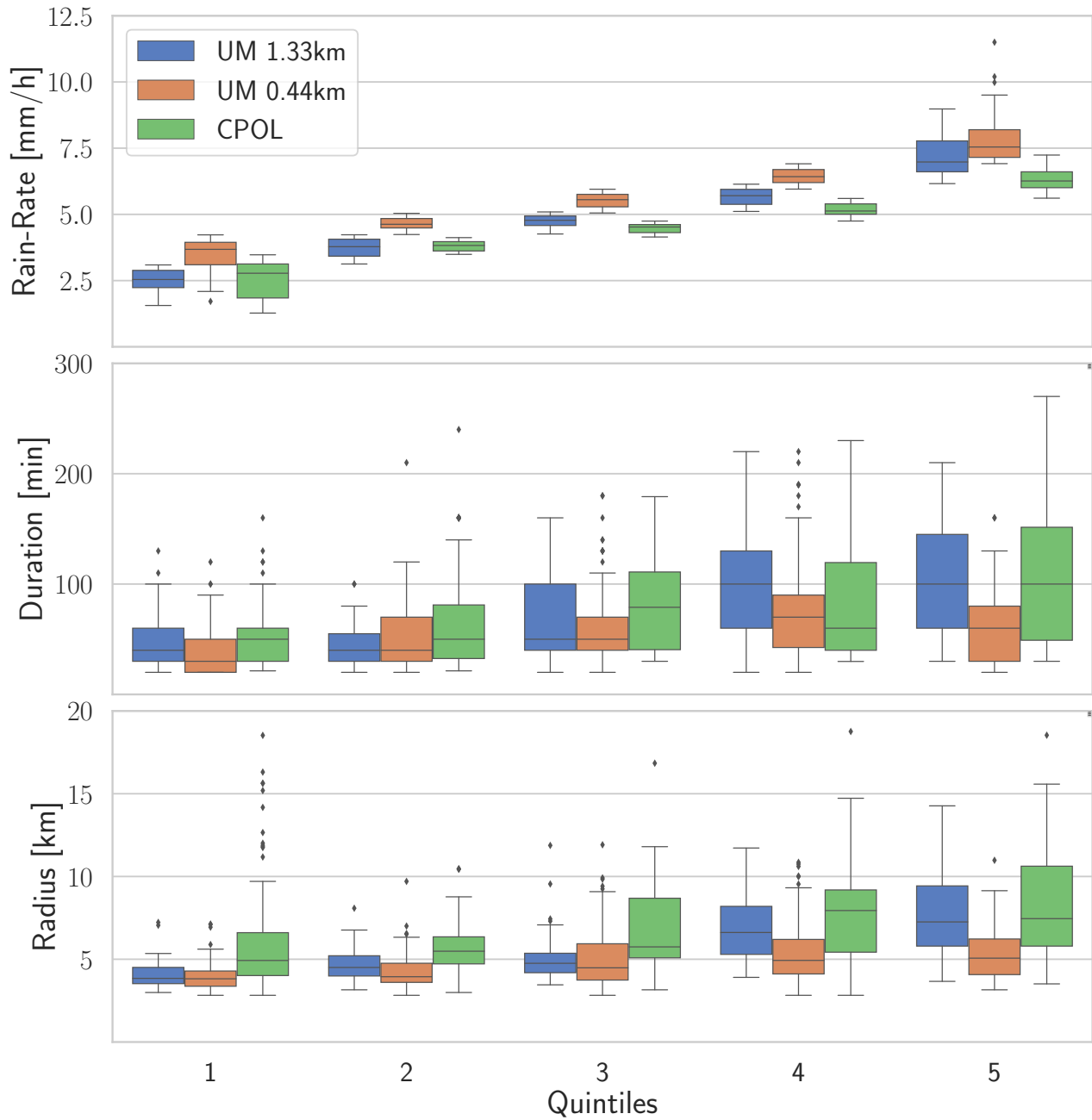


Figure 6. Storm track properties grouped by rain-rate intensities (quintiles).

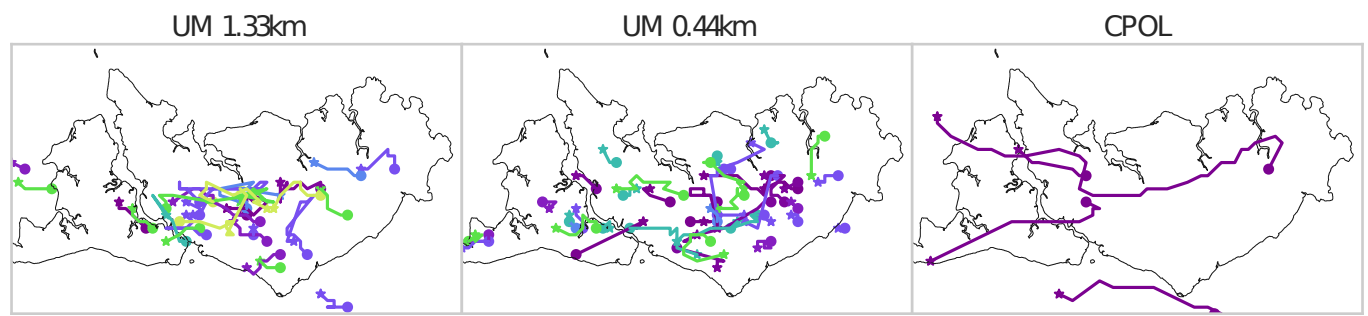


Figure 7. Storm tracks with intensities of the 5th quintile. Colors in the model data represent different ensemble members. Start of the storm tracks are indicated by a • and their end point by *

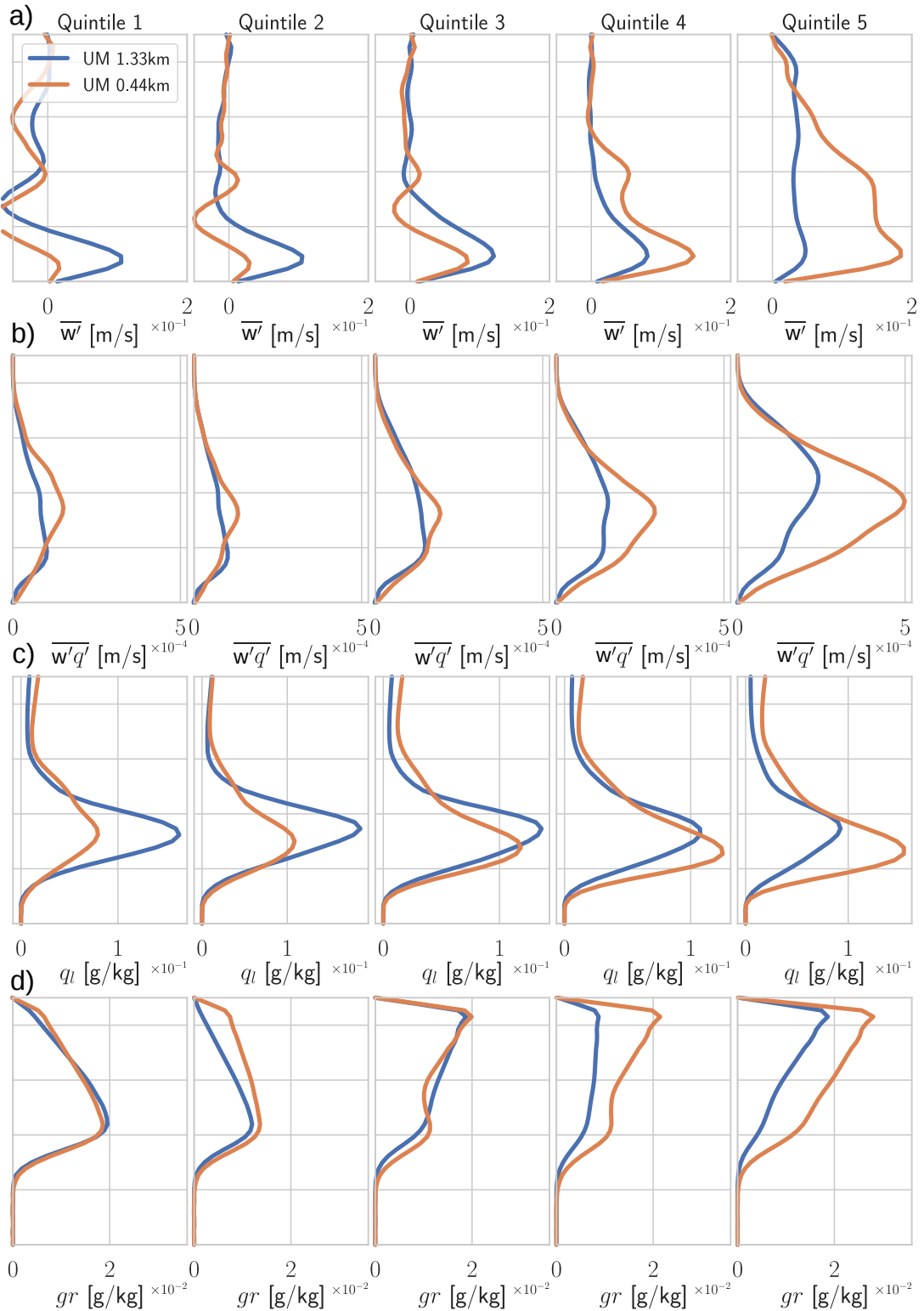


Figure 8. Average vertical profiles of a) of vertical motion fluctuations b) vertical moisture flux fluctuation, c) Cloud liquid water content d) graupel concentration grouped by storm intensity. The storm intensities are based on rain-rate quintiles.

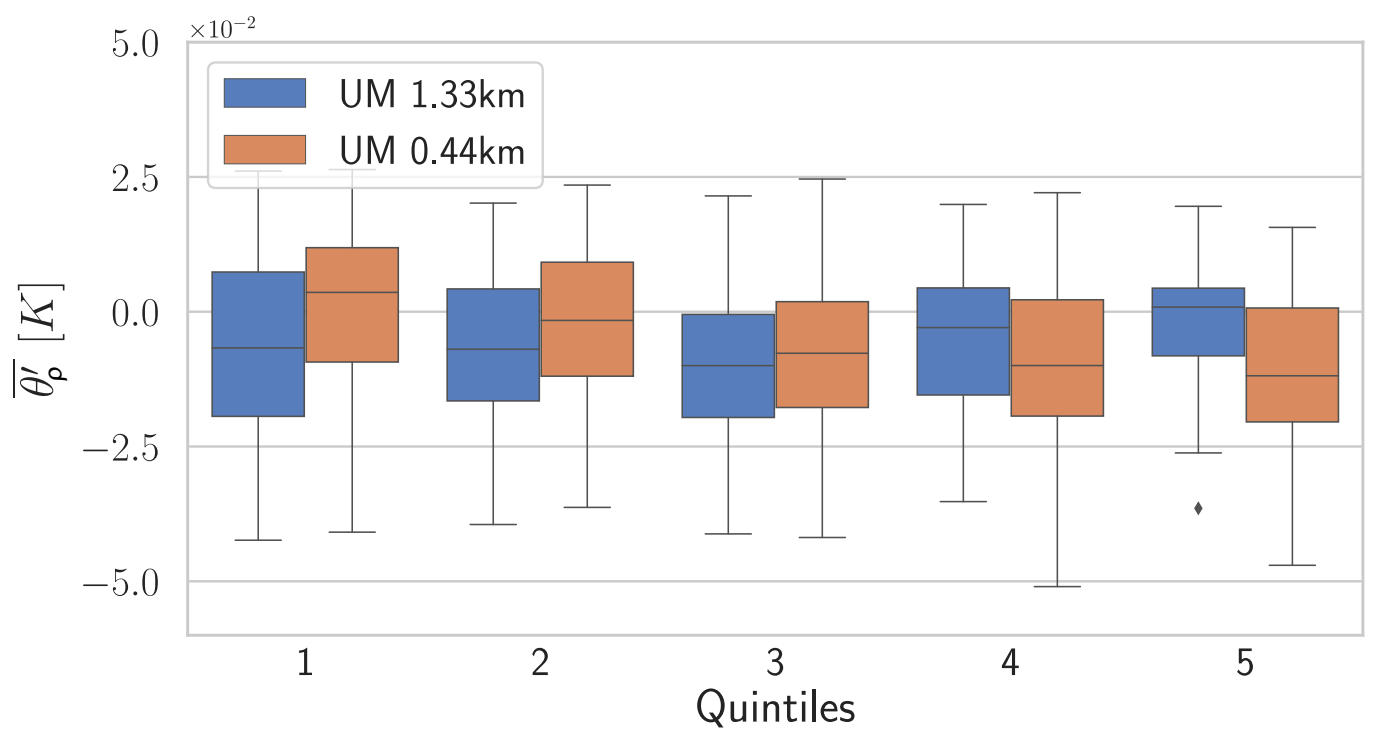


Figure 9. Distribution of field perturbations of density potential temperature.

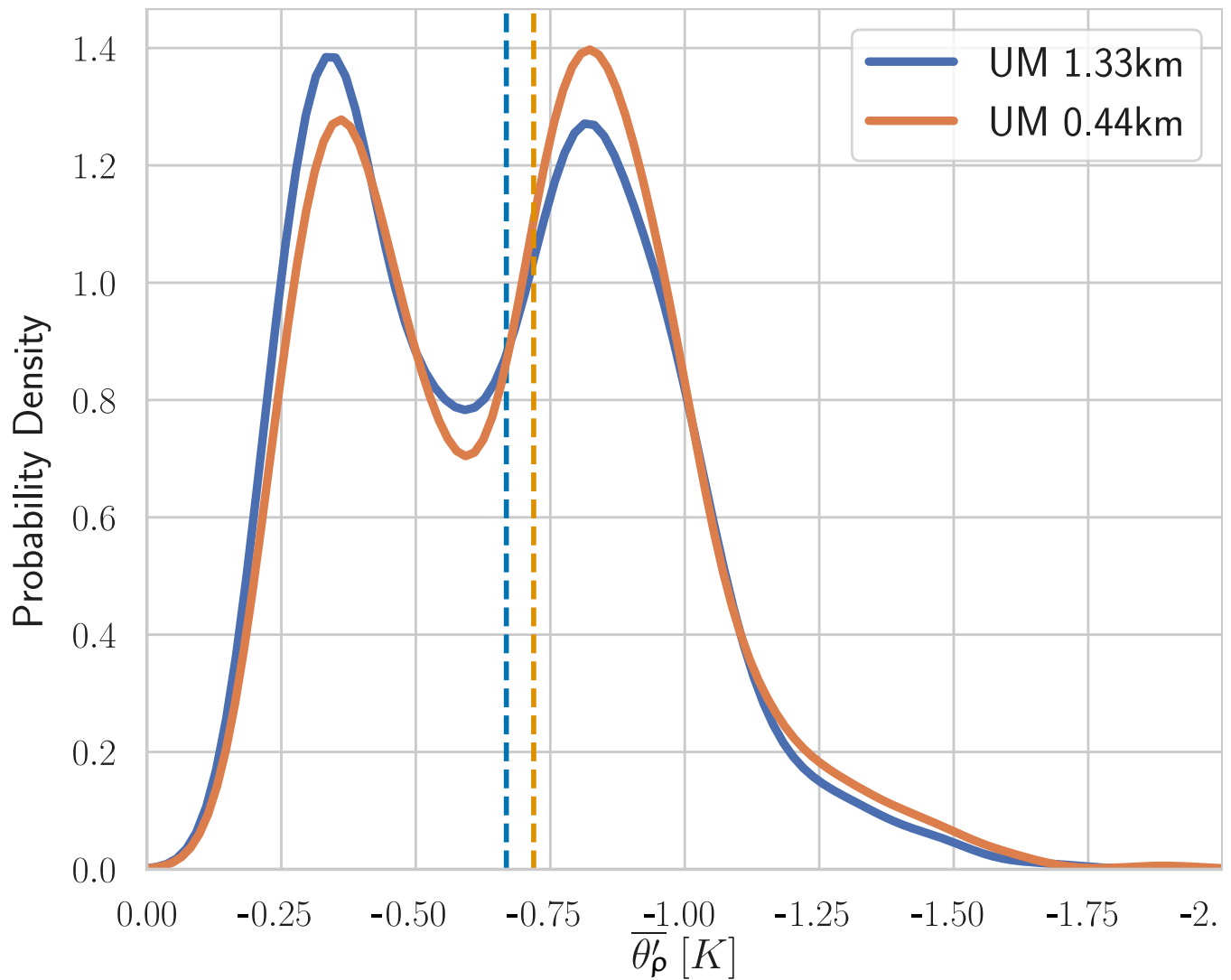


Figure 10. Comparison of the probability density of cold-pool strength, indicated by the field perturbation of density potential temperature ($\overline{\theta'_\rho}$). The medians are shown by the dashed lines.